Large eddy simulation of transverse single/double jet in supersonic crossflow

ZHAO, M., BIAN, Y., LI, Qinling <http://orcid.org/0000-0002-7191-9538> and YE, T.

Large Eddy Simulation of Transverse Single/Double Jet in Supersonic Crossflow

Majie Zhao[a], Yifang Bian[a], Qinling Li[b] & Taohong Ye[a,*]

[a] Department of Thermal Science and Energy Engineering, University of Science and Technology of China, Hefei, 230027, P.R. China

b Department of Engineering and Mathematics/MERI, Sheffield Hallam University, S1 1WB, United Kingdom

Abstract

In this paper, large eddy simulation of transverse sonic single/double hydrogen jets into supersonic Mach 2 crossflow have been carried out to investigate the complex flow structures and the mixing performance. Detailed turbulence characteristics, in terms of the instantaneous and mean flow fields, the vortex structures and their evolutions, the turbulence kinetic energy and the Reynolds shear stress distributions, the maximum hydrogen mass fraction and jet penetration, have been provided. Results of the two-dimensional and three-dimensional streamlines illustrate that the trailing counter-rotating vortex pairs (TCVP), the secondary TCVP of primary jet and the horseshoe vortex can merge and form a new horseshoe vortex. Three counter-rotating vortex pairs (CVP) are formed in the downstream of secondary jet: the CVP-B due to interactions between the supersonic crossflow and secondary jet; the CVP-C due to interactions between the supersonic crossflow, primary and secondary jets; and the CVP-D due to interactions of the supersonic crossflow and primary jet. The presence of primary jet flow alters the Reynolds shear stress distributions after the secondary injection with the influence of these large-scale structures. In addition, the two-stage jet injection system is proved to yield a better mixing performance than the single jet system.

Introduction

The fuel jet in supersonic cross-flow (JISCF), a typical combustor designed for high efficient mixing and combustion in scramjet engines, has been studied by many researchers [1-10]. The

interactions between the fuel jet plume, the large-scale coherent structures and the shock waves in a scramjet combustor, have significant effects on the mixing process and flame stabilization [11]. Moreover, a JISCF combustion chamber with multi-stage injection orifices at different stream-wise locations is found to be more effective for mixing process compared with a single fuel injection system.

In a JISCF combustion chamber with multi-stage injection orifices, the main factors affacting the mixing and combustion efficiency are the position, mass flow rate, jet-to-crossflow momentum flux ratio, injection angle of each injection orifice [2, 4-6, 8-9]. The effects of the injection angles and jet-to-crossflow momentum flux ratios of different injection orifices on the mixing process in multi-stage injection system have been reviewed by Huang [4 & 5]. They point out that the mixing efficiency is enhanced with the increasing jet-to-crossflow momentum flux ratio of the primary fuel jet. For a relatively simple two-stage injection system, the blockage effect of the primary fuel jet has a great impact on the secondary injection flow. The influence of the jet-to-crossflow momentum flux ratio and the distance between the two fuel injection orifices on the mixing and combustion characteristics have been investigated by Lee [9 & 11] using a Reynolds-averaged Navier-Stokes (RANS) approach. The mixing efficiency and jet penetration are found greatly improved from their studies. They also address that there exists an optimal injection distance, which increases with the jet-to-crossflow momentum flux ratio. However, it is worth to note that the two-stage injection system can significantly induce the stagnation pressure losses. The study of the combustion characteristics [11] suggests that the two-stage injection achieves a higher combustion efficiency and flame height than those in the single stage injection. Due to the preheating of the primary jet combustion, the Mach disk in the secondary jet is larger than that in the non-combustion one. Besides, a longer optimal injection distance is found in the primary jet combustion than that in the non-combustion flow field.

Takahashi et al. [12] studies the mixing efficiency and penetration in a supersonic transverse multi-stage injection system by using an extended fluorescence ratio technique and demonstrates that a staged-injection scheme can significantly increase the jet penetration. The further study of Takahashi et al. [13] suggested that secondary injection influenced the large-scale structure in size and inclination angle. The PDF contour clearly exhibits an intermittent feature of the large-scale turbulent behavior, which indicates an effective mixing enhancement of the staged-injection. Effects of the number of the injection orifices on the fuel jet mixing efficiency and penetration have been addressed by Pudsey et al. [14], which suggests that there is an optimal solution for the number of injection orifices. The further numerical investigation by Pudsey et al. [15] indicates that each injection orifice has contributed to the formation of the counter-rotating vortex pairs (CVP) in its downstream. Micka et al. [16] studies the combustion characteristics of a dual-mode scramjet combustor with a cavity flame holder. The results illustrate that the combined structure of the two-staged injection and a cavity is conducive to flame stability. Gerdroodbary et al. [17 & 18] adopted a fuel-air multi-stage injection system to study the mixing process. The results prove that the system can increase the fuel-to-oxidant contact area, the penetration of the fuel jet and the mixing efficiency, however it increases the stagnation pressure loss significantly.

Based on the above literature reviews, the two-staged injection has advantage for the mixing efficiency and jet penetration compared with the single injection. However, limited work has been carried out in terms of the turbulence behavior and unsteady feature with the supersonic transverse two-staged injection. Thus in this paper, large eddy simulation (LES) is employed to investigate the turbulence behaviors and unsteady features of the transverse two-staged injection into a combustion chamber, by particularly focusing on the interaction between the two-staged injections, large-scale

structures and turbulence transport characteristics in the non-reacting case. The article is organized as follows: “Computational Model and Grid Independence Verification” is introduction at the beginning. The LES results of transverse sonic single/double hydrogen jets into supersonic crossflow are presented in “Results and discussion”. Finally, the main conclusions are summarized in “Conclusion”.

2. Computational Model and Grid Independence Verification

2.1 Computational Model

Fig. 1 (a) depicts the computational domain of the single jet in crossflow. The static pressure and temperature of the perpendicular wall sonic hydrogen jet are 1126.3kPa and 500K, which are similar to the conditions considered in the previous RANS study [9]. The Mach number, static pressure and static temperature of the supersonic crossflow are 2.0, 146.6KPa and 1081K, respectively. The jet to crossflow momentum ratio J, defined as $J = \rho_j U_j^2 / \rho_\infty U_\infty^2$, is 2.0. The computational domain is -10 < x/D <25 in the stream-wise (x) direction, 0 < y/D <12 in the normal (y) direction, and -8 < z/D <8 in the span-wise (z) direction, respectively, where the fuel jet diameter D is 3.18mm.

Based on the single injection and the previous two-stage injection into supersonic combustion chamber studies [9 & 11], Fig. 1 (b) represents the computational domain schematic of the two-stage injection designed hereby. The origin of coordinates is located in the midpoint of the line that connects the two injection orifice centers, and the distance between them is 6D by comprehensive consideration of the case D3 mixing efficiency and total pressure loss in Ref [9 & 11]. The computational domain is -13 < x/D <25 in the stream-wise (x) direction, 0 < y/D <12 in the normal (y) direction, and -8 < z/D <8 in the span-wise (z) direction, respectively. For each injection orifice, the diameter is $\sqrt{2}/2$ D and the fuel mass flow rate is half of the value in the single jet, so that each jet to crossflow momentum

ratio is 2.0. The detailed flow conditions of the supersonic crosslow air and the hydrogen jet of the two test cases, the single jet and double jet, are given in Table 1.

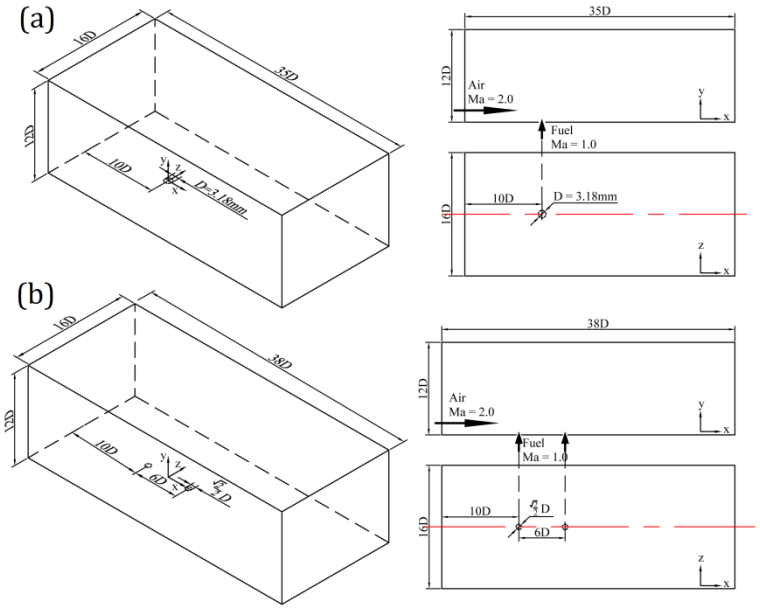

Fig. 1. Schematic of the computational domain.

Table 1 Inflow boundary conditions.

——	Ma	Pa/kPa	Ta/K	Y(H2)	Y(O2)	Y(N2)
Single Jet	1.0	1126.3	500	1.0	0	0
Double Jet	1.0	1126.3	500	1.0	0	0
Cross-flow Air	2.0	146.6	1081	0	0.232	0.786

2.2 Governing Equations

The filtered non-reactive LES compressible governing equations are

$$\frac{\partial \bar{\rho}}{\partial t} + \frac{\partial \bar{\rho}\tilde{u}_j}{\partial x_j} = 0, \tag{2.1}$$

$$\frac{\partial \bar{\rho}\tilde{u}_i}{\partial t} + \frac{\partial \bar{\rho}\tilde{u}_i\tilde{u}_j}{\partial x_j} = -\frac{\partial \bar{p}}{\partial x_i} + \frac{\partial}{\partial x_j}\left(\bar{\tau}_{ij} - \tau_{ij}^{sgs}\right), \tag{2.2}$$

$$\frac{\partial \bar{\rho}\tilde{Y}_m}{\partial t} + \frac{\partial \bar{\rho}\tilde{u}_j\tilde{Y}_m}{\partial x_j} = \frac{\partial}{\partial x_j}\left[\bar{\rho}D\frac{\partial \tilde{Y}_m}{\partial x_j} - \tau_{\tilde{\phi}}^{sgs}\right] \quad (m = 1, \cdots, N), \tag{2.3}$$

$$\frac{\partial \bar{\rho}\tilde{E}}{\partial t} + \frac{\partial}{\partial x_j}\left[(\bar{\rho}\tilde{E} + p)\tilde{u}_j\right] = \frac{\partial}{\partial x_j}\left[\lambda\frac{\partial \tilde{T}}{\partial x_j} + \tilde{u}_j\bar{\tau}_{ij} - H^{sgs} - \sigma^{sgs}\right], \tag{2.4}$$

where $\bar{\rho}$ and $\bar{p}$ are filtered density and pressure. $\tilde{u}_{j(j=1,2,3)}$ is the filtered velocity component. The filtered viscous stress tensor $\bar{\tau}_{ij}$ is computed by using the filtered strain rate tensor $\tilde{S}_{ij}$. $\widetilde{Y_m}$ is the

filtered mass fraction of species m and D is the molecular mass diffusivity. The molecular mass diffusivity is $D = \mu/\rho Sc$ [19-20], where $\mu = \frac{A_s\sqrt{T}}{1+\frac{T_s}{T}}$ is the dynamic viscosity by using Sutherland's law and Sc is Schmidt number. $\tilde{E} = \tilde{e} + \frac{1}{2}\tilde{u}_j^2 + k^{sgs}$ is the filtered total energy. λ is the molecular thermal diffusivity, $\lambda = \mu C_p/Pr$, where laminar Prandtl number $Pr = 0.72$. The relation between pressure and temperature is assumed by the perfect gas state equation

$$\bar{P} = \bar{\rho} R(\tilde{Y}_m)\tilde{T}, \tag{2.4}$$

where $R(\tilde{Y}_m)$ is the mixture gas constant.

Various SGS closure models have been discussed in the literature [21] and the sensitivity study was carried by Toda et al. [22]. In the present studies, the sub-grid scale terms are closed by the Wall-Adapting Local Eddy-viscosity (WALE) model [23]. The sub-grid enthalpy flux H^{sgs} and the sub-grid viscous work σ^{sgs} in Eqs. (2.4) are closed as

$$H^{sgs} + \sigma^{sgs} = -\frac{\mu_t C_p}{Pr_t}\frac{\partial \tilde{T}}{\partial x_j} - (\mu_t + \mu)\frac{\partial k^{sgs}}{\partial x_j} + \tilde{u}_i \tau_{ij}^{sgs} \tag{2.5}$$

where the sub-grid kinetic energy and viscosity are modeled by $k^{sgs} = C_I \Delta^2 \left(\overline{OP}\right)^2$ and $\mu_t = \bar{\rho} C_D \Delta^2 \overline{OP}$ respectively . $\Delta = \sqrt[3]{\Delta_x \Delta_y \Delta_z}$ is the filter width and $\overline{OP} = \frac{\left(S_{ij}^d S_{ij}^d\right)^{3/2}}{\left(\tilde{S}_{ij}\tilde{S}_{ij}\right)^{5/2} + \left(S_{ij}^d S_{ij}^d\right)^{5/4}}$ and $S_{ij}^d = \tilde{S}_{ik}\tilde{S}_{kj} + \widetilde{\Omega}_{ik}\widetilde{\Omega}_{kj} - \frac{1}{3}\delta_{ij}[\tilde{S}_{mn}\tilde{S}_{mn} + \widetilde{\Omega}_{mn}\widetilde{\Omega}_{mn}]$, in which $\tilde{\Omega}_{ij}$ is the anti-symmetric part of $\nabla\tilde{u}$. And $\tau_{ij}^{sgs} = \mu_t(2\tilde{S}_{ij} - \frac{2}{3}\delta_{ij}\tilde{S}_{kk})$. The turbulent Prandtl number is set as $Pr_t = 0.9$ and the model coefficients C_I and C_D are determined by a dynamic procedure [22]. The sub-grid scalar stresses are approximated using an eddy-diffusivity model, which is written as,

$$\tau_{\tilde{\phi}}^{sgs} = \left(\bar{\rho}\widetilde{u_j Y_m} - \bar{\rho}\tilde{u}_j\tilde{Y}_m\right) = -\bar{\rho}\widetilde{D_t}\nabla\tilde{\phi} \tag{2.7}$$

where $\widetilde{D}_t$ is the turbulent diffusivity modeled as $\bar{\rho}\widetilde{D}_t = \mu_t/Sc_t$, The turbulent Schmidt number is set as $Sc_t = 0.7$.

A multi-component LES numerical solver is developed based on the OpenFOAM platform for the

current numerical simulations. The numerical discretization methods are consistent with the previous literature, which have been validated [24 & 25]. The convective fluxes are reconstructed using a second order (flux limiter-based) TVD scheme and the viscous diffusion fluxes are implemented using the second order central differencing scheme. An explicit modified fourth order Runge-Kutta scheme with low storage requirement [26] is used for time integration. Generally, higher order methods can achieve more accurate results [27 & 28]. The current jet to cross flow LES accuracy has been justified by various approaches, such as controlling mesh refinement, y+, oncoming boundary conditions, energy spectra and the turbulence resolution criterion ME before the bow shock, which will be presented in the following section.

The boundary conditions are set based on the parameters provided in Table 1. An adiabatic no-slip wall boundary condition is employed at walls. For the outlet boundary, a non-reflective condition is utilized. A periodic boundary condition is applied for the spanwise boundaries. The fuel jet inlet velocity profile is prescribed by a hyperbolic-tangent function [29],

$$\frac{\tilde{u}}{U_j} = \frac{1}{2}\left\{1 - \tanh\left[\frac{1}{4\theta_0}\left(\frac{r}{r_0} - \frac{r_0}{r}\right)\right]\right\} \tag{2.8}$$

where, U_j is the velocity at the center of the injection orifice, $r = \sqrt{y^2 + z^2}$, r_0 is the jet radius, and the initial momentum thickness θ_0 is 0.045D in the current simulations [30]. The mean velocity of supersonic crossflow inlet is computed from an additional RANS simulation, and the turbulent fluctuation velocity is computed by a synthetic turbulence inlet boundary condition based on the digital filtering[31].

2.3 Computational Grid and Verification

Fig. 2 shows the computational grid topology of the transverse double jet in supersonic crossflow. Hexahedral meshes are utilized for all cells, and O-type gird is employed for the fuel injection. For

mesh used in the present simulations, the detailed information of the mesh is shown in Table 2. In order to improve the simulation accuracy, grid refinement is performed particularly near the wall and the injection orifice to ensure $y^+ \leq 1$ for the first grid adjacent to the wall. Moreover, the growth ratio of the mesh from the wall is 1.05. It should be noted that the grid independence analysis is only performed for the double jet simulations considering the cost of LES calculation in the present study.

Table 2. The detailed information of mesh generation.

Case	$N_x \times N_y \times N_z$	Total number	y^+
Double jet	301×161×101	= 4.8 million	3.3 ~ 5
	401×251×151	= 15 million	1.4 ~ 3
	631×321×241	≈ 48.38 million	⩽ 1
Single jet	551×321×241	≈ 42.37 million	⩽ 1

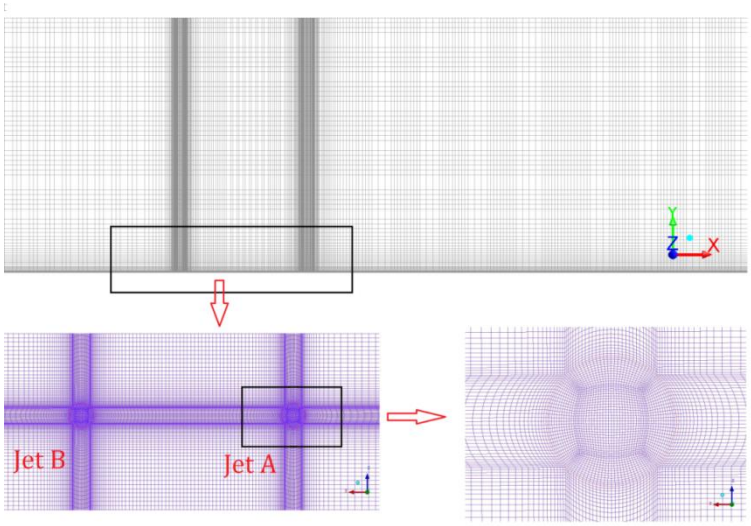

Fig. 2. Grid topology of the current study.

According to Pope [32], at least 80% of the total turbulence kinetic energy (TKE) being resolved indicates a well-resolved LES. The well-established turbulence resolution criterion is defined as,

$$Me = \frac{k_{sgs}}{k_{RES} + k_{sgs}} \tag{2.9}$$

where k_{sgs} is the sub-grid turbulence kinetic energy and k_{RES} is the resolved turbulence kinetic

energy.

$$k_{RES} = \frac{1}{2}\langle\langle\tilde{u}_i^2\rangle - \langle\tilde{u}_i\rangle^2\rangle \tag{2.10}$$

where $\langle\cdot\rangle$ represents an ensemble averaging. Fig. 3 provides the distributions of Me of the transverse single/double jet in supersonic crossflow, which is computed using the data where hydrogen exists. As seen in Fig. 3, the results show a good coherence with the well-established turbulence resolution criterion, $Me \ll 0.2$ which means that the fine grid is able to predict the characteristics of the inertial subrange [32]. Mean streamwise and normal velocity profiles between the injections of transverse double jet in supersonic crossflow (x/D=0, z/D=0) are presented in Fig. 4 (a) and (b) for the grid sensitivity analysis. Moreover, mean stream-wise velocity in semi-logarithmic scale downstream of the supersonic crossflow inlet 5D and turbulence energy spectrum in the jet shear layer (x/D = 0, y/D = 2 & z/D = 0) are also ploted in Fig. 4. Results indicate a reasonable convergence for grid resolution. Therefore, the unsteady turbulence structures and fluctuations in the flow field can be well captured with the current computational grid. Moreover, it should be noted that the present numerical strategy is mainly focus on the large scales and mixing in the near field of injection and the detailed mixing predictions may not be well done far from the injections.

The marching time-step is adjusted based on the Courant number under 0.2 to capture the unsteady flow structure. For each case, four flow through times (4 L/U) is run to ensure a statistical stationary, where L is the streamwise computational domain length and U is the air inlet mean velocity. Time-averaging is performed with about six flow through times (6 L/U), and the statistical convergence can be conformed by the time shifting average as seen in Fig 4 (a) and (b), where t1 is about four flow through time (4 L/U) and t2 is about six flow times (6 L/U). In addition, the numerical methods used in this paper have been well validated in the previous studies [24-25].

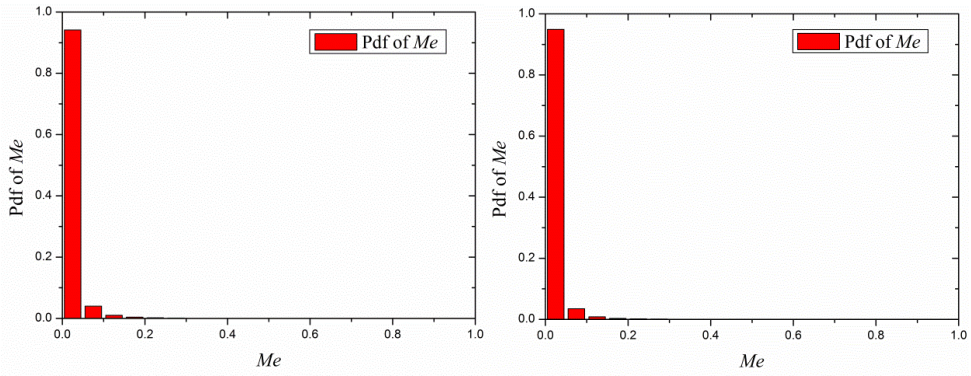

(a) Distributions of *Me* of the transverse single jet in supersonic crossflow

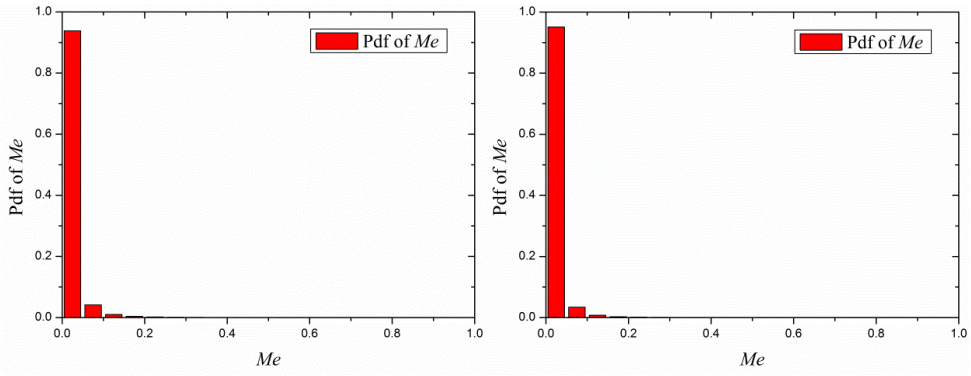

(b) Distributions of *Me* of the transverse double jet in supersonic crossflow

Fig. 3. Probability density distribution of *Me* at two different instantaneous time.

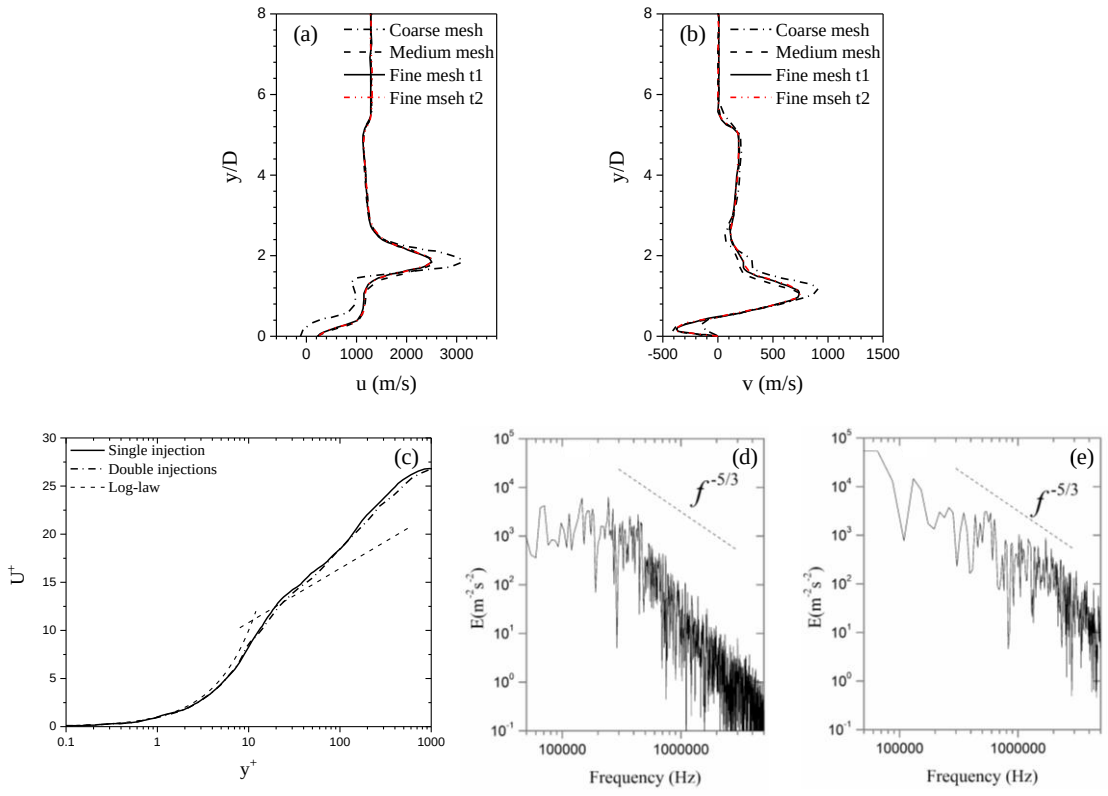

Fig. 4. Mean streamwise (a) and normal (b) velocity profiles between the injections of transverse

double jet in supersonic crossflow (x/D=0, z/D=0) with different grids and statistical time; (c) Mean stream-wise velocity in semi-logarithmic scale downstream of the supersonic crossflow inlet 5D; Turbulence energy spectrum in the jet shear layer (x/D = 0, y/D = 2 & z/D = 0): (d) transverse single jet in supersonic crossflow, (e) transverse double jet in supersonic crossflow.

3. Results and Discussion

3.1 Instantaneous Flow Field

Fig. 5 shows the instaneous numerical schlieren $\|\nabla\overline{\rho}\|$ in the central plane (z/D=0) for the two cases, single jet and double jet, where t1 and t2 are the moment after statistics steady respectively. As shown in Fig. 5 (a) for single injection, the under-expanded fuel jet fluid passes through the Prandtl-Meyer Expansion Fan (PMEF) near the fuel injection and is accelerated to supersonic state. And the fuel jet fluid is then compressed leading to a barrel shock and a Mach disk. Due to the blockage of the fuel jet fluid, a bow shock is formed around the windward side of the fuel jet. The bow shock/boundary layer interactions cause the separation shock and separation region upstream of the fuel injection. The formation of the reflected shock at the junction of barrel shock and Mach disk is due to the blockage of jet, and more than one reflected shock waves appear on the windward side of the barrel shock, which is consistent with the observation by Ben-Yakar et al. [33]. The junction of the Mach disk, barrel shock and reflected shocks is called a triple point. The large scale shear layer vortex structures originate from the interaction between the bow shock and barrel shock. These large scale vortex structures can cause acoustic shock after bow shock, which eventually merges with the bow shock and causes the oscillation of bow shock [34]. It is worth to point out that the large-scale shear layer vortex structure is generated on the windward side of the barrel shock wave, while the small-scale vortex structure generated on the leeward side of the barrel shock is related to the boundary layer separation.

Fig. 5 (b) shows the numerical schlieren $\|\nabla\overline{\rho}\|$ of the double jet case. The flow structures near the

primary injection are nearly the same with that generated by the single injection. However, significant different flow structure can be observed near the secondary fuel injection due to the influence of primary injection on the secondary injection. The large scale jet shear vortex generated by the primary fuel jet directly destroys the bow shock structure upstream of secondary fuel injection. The small-scale vortex structures generated on the leeward side of primary injection influence the base of the bow shock and the generation of secondary jet shear layer. Thus, it forms a much complex vortex structure on the upstream side of secondary injection. Due to the influence of the primary jet fluid flow, the acoustic shock that originally exists behind the bow shock is relatively weak, which even disappears near the secondary fuel jet. Although the bow shock of the secondary injection is destroyed, the barrel shock still exists clearly, and becomes smaller compared to the single injection, which in turn causes the height of the Mach disk to decrease. In addition, the secondary jet shear layer vortices interacts with that of primary jet shear layer on the windward side. And the two jet shear layer vortices merge downstream, resulting in much more complex shear layer vortex structure. In addition, the three-dimensional instantaneous vorticity fields in terms of the Q-criterion isosurface ($Q=10^{11}$) coloured by H2 mixture fraction are also shown in Fig. 5 (c for single injection) and (d for double injection). It can be seen that much more fine vortex structures around and downstream of secondary injection are observed. These suggest a significant mixing enhancement of fuel and air, which will be quantitatively analyzed in the following sections.

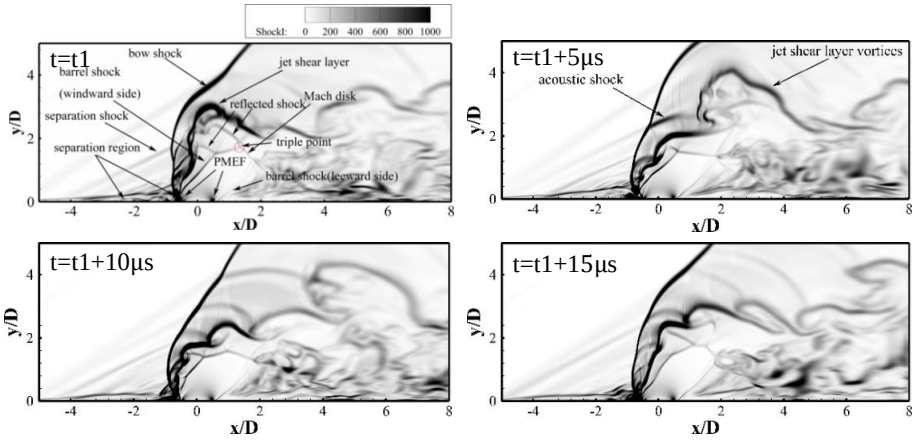

(a) Single injection

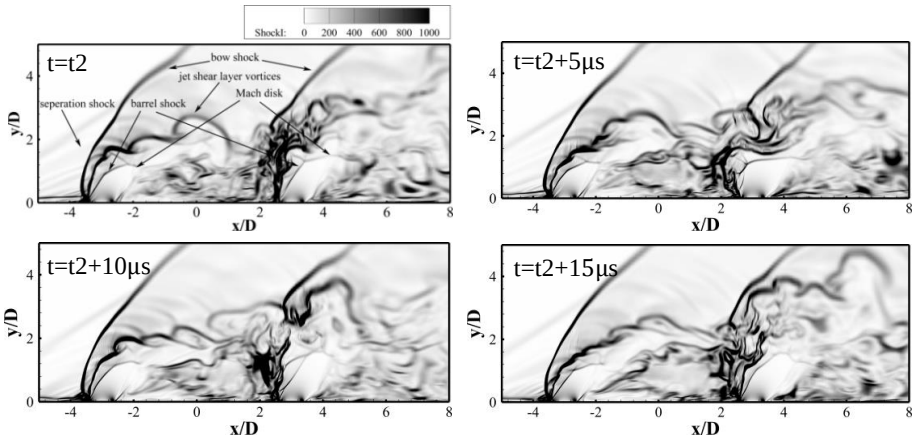

(b) Two-stage injection

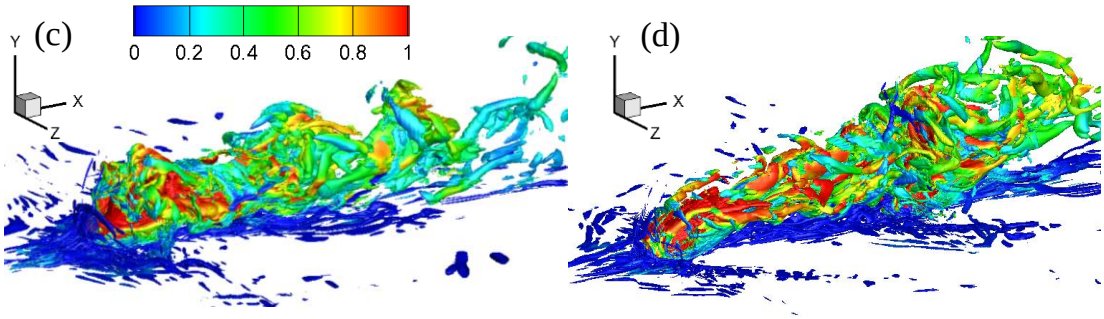

Fig. 5. Numerical Schlieren $\|\nabla\overline{\rho}\|$ of different instants in the central plane (z/D=0) and the three-dimensional instantaneous vorticity field in terms of the Q-criterion isosurface ($Q=10^{11}$) coloured by H2 mixture fraction, (a & c): single injection, (b & d) two-stage injection.

3.2 Mean Flow Field

The distributions of Mach number, streamline and the hydrogen mass fraction in the central plane (z/D=0) of the single/double injection cases are shown in Fig. 6. Three recirculation zones are formed in the single injection case as seen in Fig. 6 (a). Along the crossflow direction are the recirculation zone

(R1) produced by the interaction of the separation shock and the boundary layer, the separation zone (R2) created by the barrel shock on the windward side, and the recirculation zone (R3) downstream of the leeward side. The supersonic crossflow is reduced to the subsonic after bow shock due to its compression. At the same time, the jet fluid is faster than the incoming fluid, thus the large-scale hovering vortex (R2) rotates in the counterclockwise direction. It is found that higher expansion of the barrel shock at the leeward side of the jet than that at the windward side, which corresponds to a larger Mach number at the leeward side. The height of the Mach disk, defined as the height between its center and the down wall, is H=1.3D.

In the two-stage injection system, the shock structures near the primary injection are similar to that in the single injection system (as seen Fig. 6 (b)). However, due to the interaction of the two injections, the adverse pressure gradient formed by the crossflow bypassing the primary injection is much higher, resulting in a larger recirculation zone (R3) in the downstream region of primary injection. Since the bow shock base of the secondary injection is affected by the primary jet fluid flow, there is only one recirculation zone (R4) induced by the boundary layer separation. And the separation zone (R2) related to the barrel shock on the windward side vanishes upstream the secondary injection. The height of the Mach disk for primary and secondary injection are H=0.9D and 1.0D respectively. From the distribution of the average mass hydrogen fraction in the central plane shown in Figs. 6(c) and 5(d), the fuel jet core region, where the mass fraction of hydrogen is close to unit, becomes smaller for the two-stage injection system. Note that the total fuel mass flow rate of the double injection case is the same as that of the single injection case, and the two-stage injection can increase the penetration of the secondary injection significantly. Although the primary jet has equal jet to crossflow momentum ratio as a single injection, the primary jet has lower penetration because the mass flow rate of the primary

injection in the two-stage injection is less than that in the single injection.

Fig. 7 exhibits the averaged temperature distributions in the central plane (z/D=0) for the two cases. It can be seen that there is a high-temperature zone after the bow shock in the single injection system, which is due to the compressibility of the bow shock and the Lambda (λ) shock. The presence of the high-temperature region is responsible for the self-ignition which plays a key role in the flame stabilization. In contrast to the single injection, there is also a high-temperature region after the bow shock on the upwind of the primary injection for two-stage injection. However, no similar high-temperature zone upstream the secondary hydrogen jet can be captured due to the influence of the primary injection. Compared with the single jet temperature, the primary core jet temperature distribution is altered significantly by the second bow shock. Fig. 7 also suggests that slight increase the distance between the two jets can increase the upward temperature of the second jet at y/D = 2, which will further stabilize the second jet flame. It is noteworthy that a higher temperature zone appears in the recirculation zone (R4), which is mainly due to the high enthalpy cross flow in this zone with lower velocity, which leads to close static temperature with the total temperature. On the other hand, some weak shock waves at the base of bow shock upstream of the secondary injection, which can be seen in Fig. 5, are also responsible for the higher temperature zone.

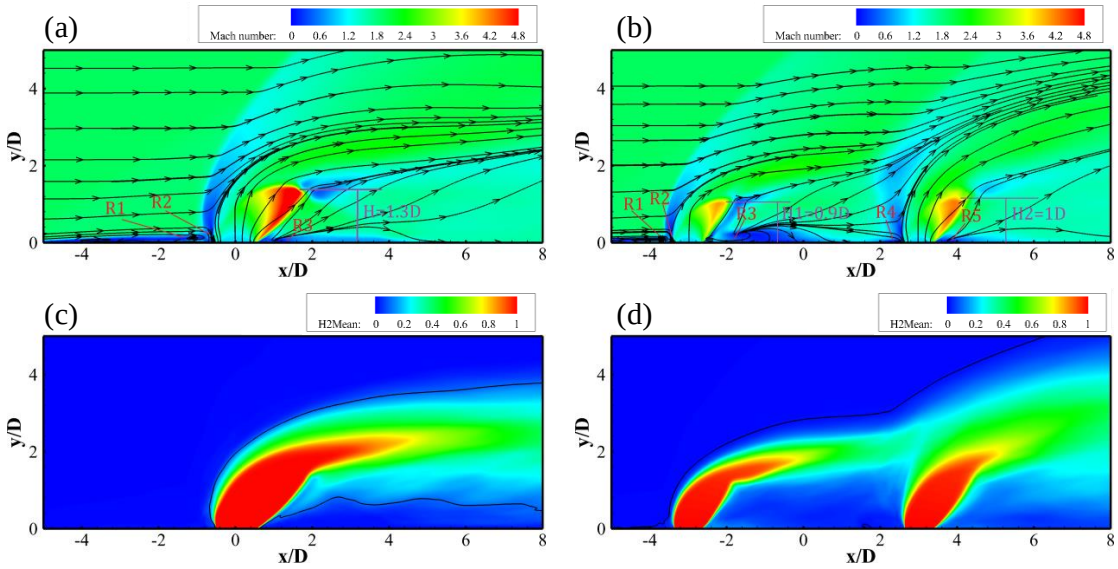

Fig. 6. Distributions of Mach number, streamline and the average hydrogen mass fraction in the central plane (z/D=0) of the single/double injection in (a) and (b); and the hydrogen mass fraction isolines of 0.01in (c) and (d).

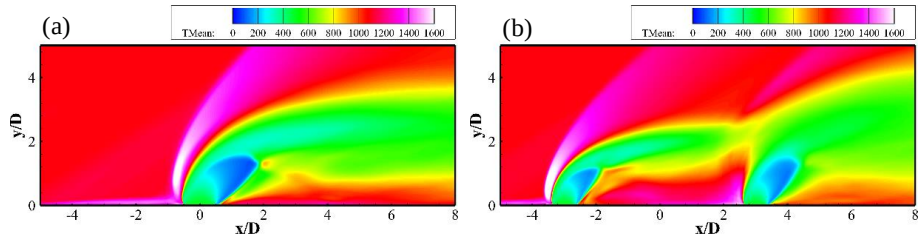

Fig. 7. Distributions of the averaged temperature in the central plane (z/D=0), (a): single Injection, (b) two-stage injection.

3.3 Three-dimensional Flow Field

Fig. 8 displays the three-dimensional averaged vorticity field in terms of the Q criterion isosurface ($Q=10^{11}$). Typical vortex structures of the single jet case can be seen in Fig. 8(a): (1) the horseshoe vortex upstream and around the hydrogen injection, corresponding to the recirculation zone R1 in Fig. 6(a); (2) the upward motion hovering vortex formed between the fuel jet and the upstream horseshoe vortex, which corresponds to the recirculation zone R2 in Fig. 6(a); (3) the counter-rotating vortex pairs (CVP) in the downstream originating in the hanging vortex on both sides of the injection; (4) a small counter-rotating vortex pair (CVP-1) formed inside the terminal of the hanging vortex due to the presence of the Mach disk; (5) the trailing counter-rotating vortex pair (TCVP) near the bottom wall,

which is related to the separation of the low pressure recirculation zone in the wake of hydrogen jet and the boundary layer separation [35].

As seen in Fig. 8 (b), the vortex structures become more complex in a two-stage injection system. They can be summerised as the following points: (1) the vortex structures of the flow field near the primary injection is similar to that in the single injection system; (2) the CVP structure downstream of the primary injection, labeled as CVP-A in Fig. 8(b), is destroyed in the upstream region of the secondary injection; (3) the CVP structure of secondary injection is formed, which will be discussed in the following section; (4) The TCVP structure (TCVP-1) of the primary injection is separated to form a secondary TCVP structure (TCVP-2) before it encounters the secondary injection. And finally, the TCVP-1, TCVP-2 and the upstream horseshoe vortex of the secondary injection merge and develop downstream along both sides of the secondary injection.

Fig. 9 constructs a 3D view of the complex flowfield: the contours of Mach number at the central plane (z/D=0), the magnitude of streamwise vorticity on the cross plane x/D=6 (where the positive and negative regions represent the direction of the vorticity), and the static pressure on the wall (y/D=0). The 3D streamlines of the mean field is also added in Fig. 9, where the streamlines of the primary jet fluid are marked with black color, the secondary jet fluid by red color, and the supersonic crossflow by other colors, respectively. In addition to the recirculation zones in Fig. 6(b), a pair of recirculation zone (R) is formed between the primary and the secondary jets. This recirculation zone results in the formation of a secondary TCVP-2 structure. According to the colorful streamlines of supersonic crossflow, the merging process of the TCVP-1, TCVP-2 and horseshoe vortex upstream of the secondary injection can be clearly visualized. Furthermore, three pairs of CVP structures are formed downstream of the secondary injection: the first one is the counter-rotating vortex pair (CVP-B) formed

by the interaction of supersonic crossflow and secondary jet fluid; the second one is the counter-rotating vortex pair (CVP-C) formed by the interaction of the supersonic crossflow, the primary jet fluid and the secondary jet fluid; the third one is the weaker counter-rotating vortex pair (CVP-D) formed by the interaction of the supersonic crossflow and the primary jet fluid, in Fig. 9. These different large scale vortex structures interact with each other to promote the mixing process of the fuel jet and supersonic crossflow. In addiction, the "V" interface region with CVP-C1 downstream and CVP-C2 upstream in a common direction of rotation but traveling in opposing directions between the two injections identified by Pudsey et al. [35] is also observed in the present simulation.

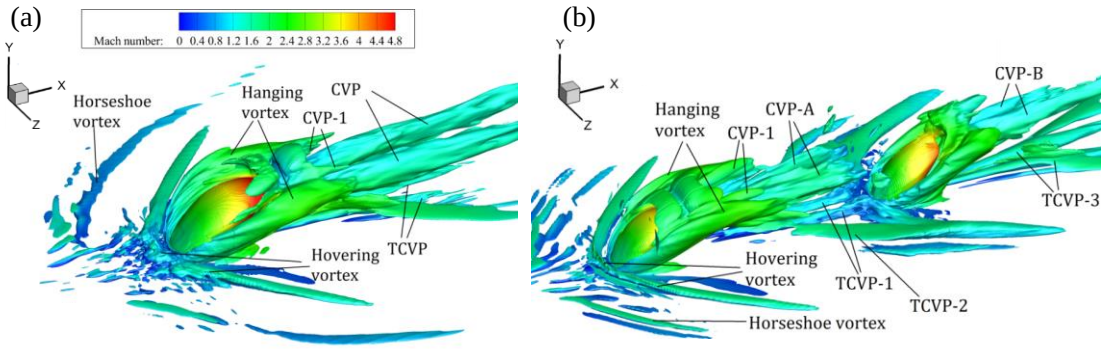

Fig. 8. Three-dimensional averaged vorticity field in terms of the Q-criterion isosurface ($Q=10^{11}$), (a): single injection, (b) two-stage injection.

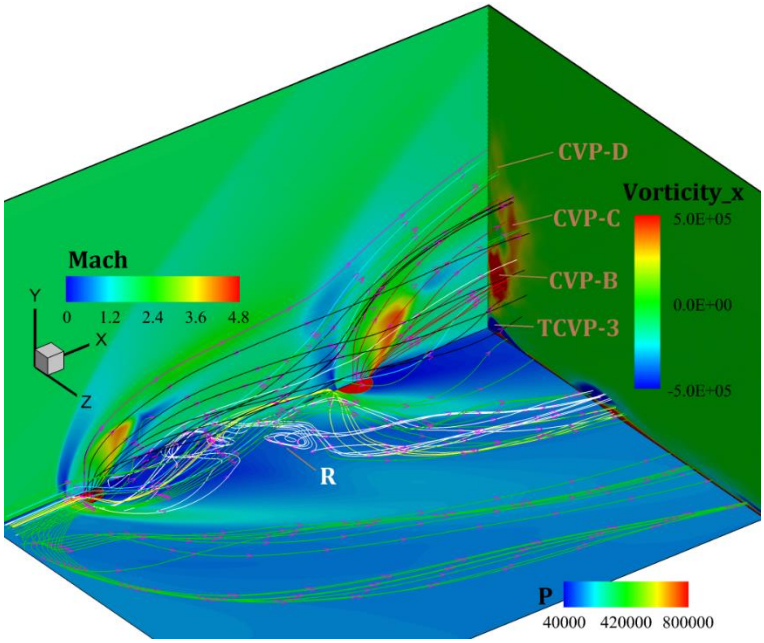

Fig. 9. Distributions of the Mach number in the central plane (z/D=0), the streamwise vorticity at the

cross plane x/D=6 and the static pressure at the wall (y/D=0).

For the single injection, Fig. 10 provides the mean Mach number and streamline distributions at x/D=0, 1, 2, 3, 4 and 5, respectively. The counter-rotating hanging vortex pair (shown in Fig. 8) on both sides of the injection can be seen in the cross plane x/D=0 and x/D=1. The high Mach number region in the x/D=1 plane is within the barrel shock. As the jet fluid develops downstream, the counter-rotating hanging vortex pair begins to shift to the CVP structure and a small counter-rotating vortex pair (CVP-1 in Fig. 8) is formed in x/D=2 and x/D=3 after the Mach disk. This small counter-rotating vortex pair (CVP-1) gradually moves upwards, and the trailing CVP structure begins to appear, and gradually become larger (see Fig.8). As the jet fluid develops further downstream, the flow field of jet plume is mainly dominated by the CVP structure in x/D=4 and x/D=5. TCVP begins to deform and increase.

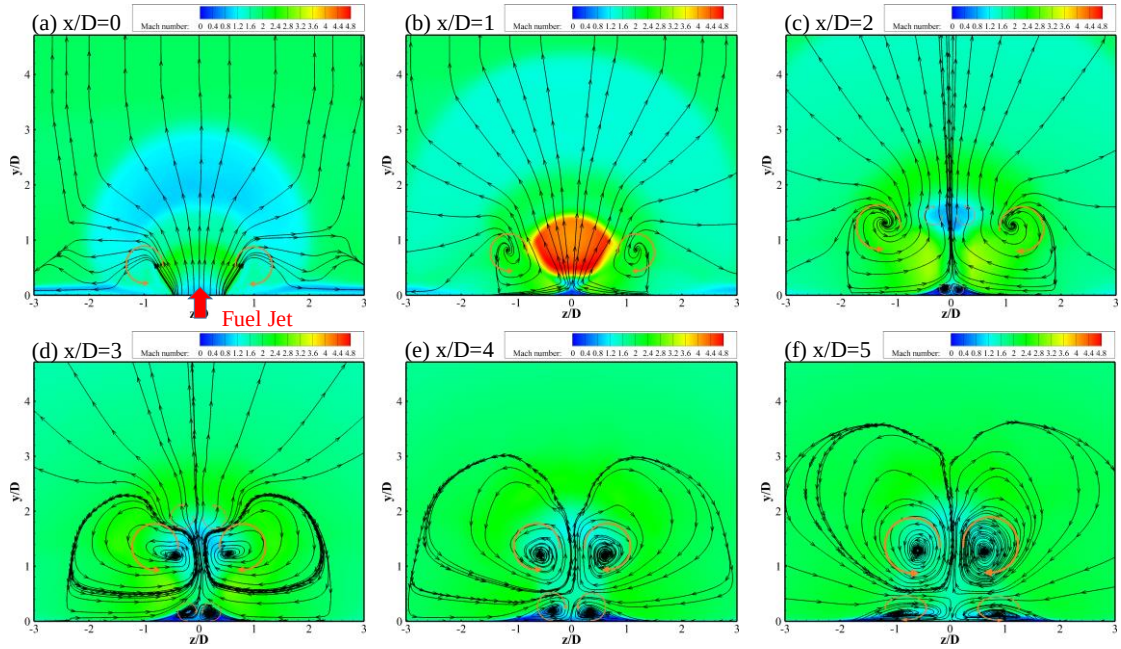

Fig. 10. Single injection Mach number and streamline distributions at x/D=0, 1, 2, 3, 4 and 5, where the fuel jet is located at x/D=0.

For the two-stage injection system, Fig. 11 illustrates the mean Mach number and streamline distributions at x/D=-3, -2, -1, 0, 1, 2, 3 and 4, respectively. Although each jet to crossflow momentum

ratio is the same to the single injection, the mass flow rate of each jet is only half of the value of the single injection, which leads to the Mach number in the barrel shock being obviously weakened and the low Mach number recirculation zone under the barrel shock wave being relatively strengthen. A pair of small counter-rotating vortices seen in the cross-section x/D=-2 is formed in the same direction of the counter-rotating hanging vortex pair. Formation of the small CVP is due to the interaction of the recirculation zone and crossflow that bypass the primary jet. With the development of the primary jet fluid, the transition of the counter-rotating hanging vortex pair to the CVP structures can be detected on the planes x/D=-1 and x/D=0. Consistent with the single injection system, a small counter-rotating vortex pair CVP-1 is formed after both sides of the Mach disk. The small counter-rotating vortex pair with the same direction of the counter-rotating hanging vortex pair increases in plane x/D=-1, and the vortex pair is merged to form the CVP slightly downstream (x/D=0). The TCVP structure begins to appear at x/D=-1. With the primary jet fluid approaching the secondary injection, the TCVP structure begins to separate and to form two TCVP structures at x/D = 1 and x/D = 2, which are marked as TCVP-1 and TCVP-2 in Fig. 8. The planes x/D=3 and x/D=4 are in the region where the primary jet fluid interacts strongly with the secondary jet fluid. The weak counter-rotating vortex pair (CVP-C, seen in Fig. 9) is formed by the interaction of supersonic crossflow, primary jet fluid and the secondary jet fluid at x/D=3. At this point, the counter-rotating hanging vortex pair of the secondary injection begins to develop and the CVP-B will be formed downstream. Consistent with the results in Figs. 8(b) and 8, TCVP-1, TCVP-2 and the horseshoe vortex of the secondary injection merge into a counter-rotating vortex pair on both sides of the secondary injection near the wall.

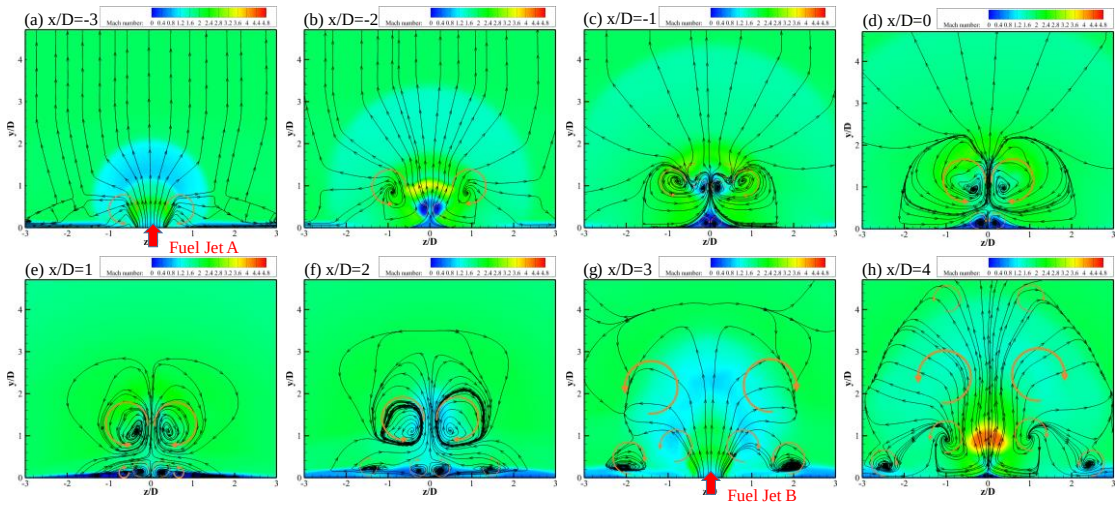

Fig. 11. Two-stage injection Mach number and streamline distributions at different streawise location (x/D = -3, -2, -1, 0, 1, 2, 3 & 4), where x/D = -3 and 3 represent the locations of primary jet and secondary jet respectively.

3.4 Statistical Characteristics of Turbulence

Fig. 12 shows the distributions of turbulent kinetic energy [$\mathrm{TKE} = (\langle u'u' \rangle + \langle v'v' \rangle + \langle w'w' \rangle)/(2U_\infty^2)$] in the central plane (z/D=0) and normal-wise plane (y/D=1) of the two cases. It can be seen that there are four regions with higher turbulent kinetic energy in the single injection system, identified by 1, 2, 3 and 4, respectively (seen in Fig. 12 (a)). Higher turbulent kinetic energy in Region 1 after the base of the bow shock is due to the large-scale vortex structures formed by adverse pressure gradient and the interaction of the bow shock and boundary layer, which agrees well with Santiago et al. [36]. The reflected shock at the end of the windward of the barrel shock is responsible for the higher turbulent flow energy Region 2. Region 3 is located on the leeward side of the barrel shock downstream of the injection. As the supersonic crossflow fluid bypasses the jet flow, an outward moving shock wave is generated, causing the fluid to move up and down and resulting in strong turbulence kinetic energy in Region 3 [29, 36]. It is worth noting that there is also a relatively high turbulence kinetic energy region with low pressure and Mach number downstream of the injection. This is because the outward moving shocks cause the separation of the wall boundary layer [34]. That

the region with higher turbulent kinetic energy appears in the downstream identified by Region 4 is because the outward moving shock becomes stronger and the CVP's entrainment effect is further enhanced downstream.

In the double injection system, the bow shock of secondary injection is destroyed by the primary jet fluid resulting in a large disturbance in the downstream, thus a higher turbulence kinetic energy appears near the secondary injection, especially in the shear layer region on the windward side as seen in Fig. 12 (b). Due to the blockage of the secondary injection, the pressure gradient distributions in the downstream region of the primary jet orifice is affected, resulting in a higher turbulence kinetic energy in the shear layer region (as the Region 4 in single injection) downstream of the primary injection. The turbulent kinetic energy in normal plane y/D=1 increases significantly.

Fig. 13 and Fig. 14 represents the turbulent kinetic energy distributions at different cross-sections of the single/double injection. The turbulent kinetic energy near the wall on both side of the secondary injection is also greatly enhanced in the double injection case. That is due to the fact that the TCVP structure of the primary injection encounters and bypasses the secondary injection on both sides, and interacts with the wall. Although the spanwise distribution of the turbulence kinetic energy in the far field downstream of the double injection is relatively reduced, the normal y direction distribution of the turbulence kinetic energy in the far field is significantly increased, i.e., the penetration is increased. In general, the turbulent kinetic energy distributions are significantly changed in the double injection system and are strongly influenced by the interaction between the primary injection and secondary injection. The higher turbulent kinetic energy contributes to the mixing process of fuel jet and supersonic crossflow.

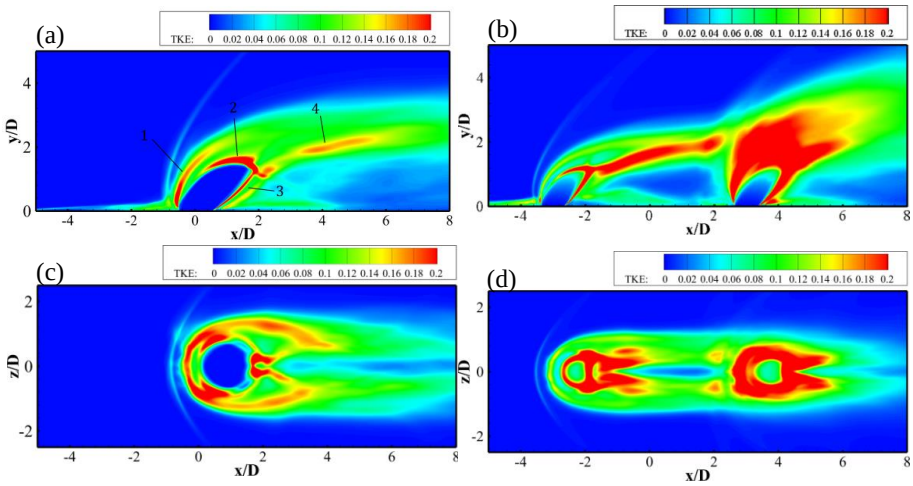

Fig. 12. Distributions of the TKE: (a) single injection at z/D = 0, (b) double injection at z/D = 0, (c) single injection at y/D = 1, (d) double injection at y/D = 1.

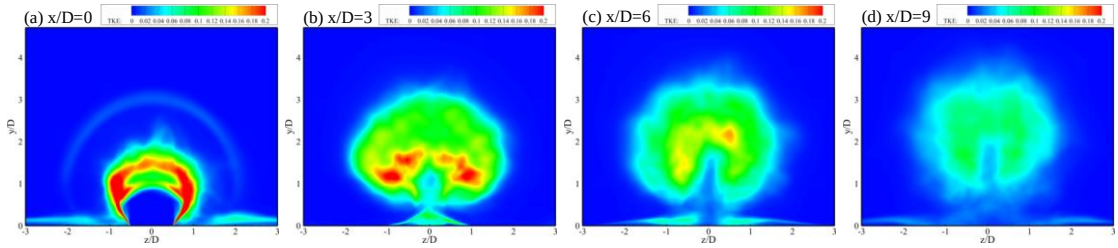

Fig. 13. The single injection TKE distribution at different cross-sections.

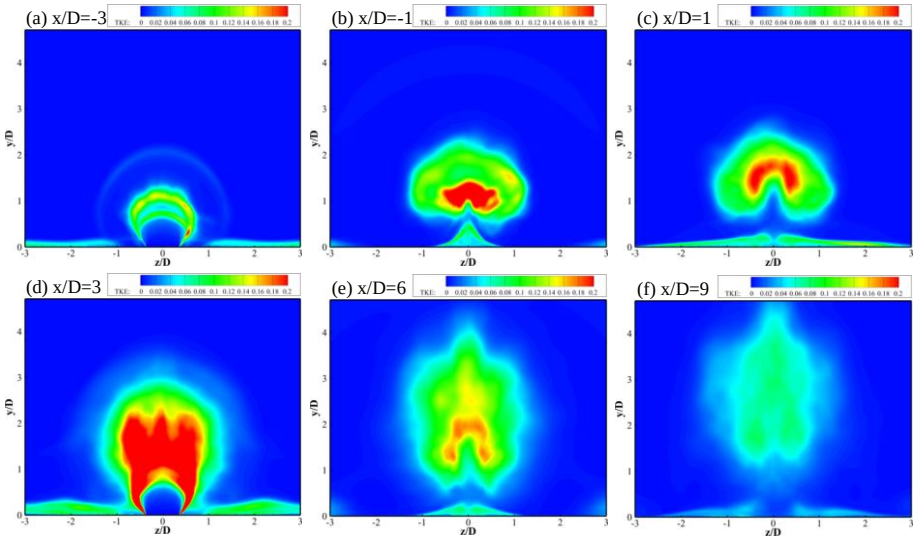

Fig. 14. The double injection TKE distribution at different cross-sections.

Turbulence statistics in terms of the Reynolds shear-stress ($RS = \langle u'v' \rangle / (U_\infty^2)$), which has important effects on the turbulent mixing [37], is an alternative way to test the single/double injection system. Fig. 15 illustrates the RS distribution in the central plane (z/D=0) and normal-wise plane (y/D=1) for the two cases. In the single injection system, two high Reynolds shear stresses regions

(RS1 and RS2) with opposite shear direction are observed upstream of the injection, similar to the results found in the experiments of Santiago et al. [36], who suggested that these two high Reynolds shears regions are related to the higher averaged velocity gradient. In addition, there is a region (RS3) with positive Reynolds shear stress in the windward jet shear layer, and a region (RS4) with negative Reynolds shear stress in the leeward jet shear layer. This negative region (RS4) is mainly due to the ring shear layer dominated by the CVP [29, 36]. There is a relatively high Reynolds shear stress near the wall upstream and downstream of the injection due to the local wall boundary layer separation. With the decrease of the velocity gradient of the supersonic crossflow and the jet flow in the downstream, the Reynolds shear stress is gradually dominated from a positive value to a negative value.

There exhibits a stronger Reynolds shear stress in the double injection system (Fig. 15 (b)). The negative Reynolds shear stress downstream of the primary injection is linked to the negative Reynolds shear stress on the windward of the secondary injection. Compared to the single injection, distributions of the Reynolds shear stress around the secondary jet the primary injection are changed by the primary injection. There is only negative Reynolds shear stress on the windward of the secondary injection, and Reynolds shear stress downstream of the secondary injection is gradually dominated by a positive value. Fig. 16 and Fig. 17 show the distributions of Reynolds shear stress in the cross-sections of the single/double injection, respectively. The transformation of the positive Reynolds shear stress region dominated by jet shear layer and the negative Reynolds shear stress region dominated by the CVP can be clearly observed. The presence of primary injection changes the distributions of Reynolds shear stress in the downstream of the secondary injection in the double injection system.

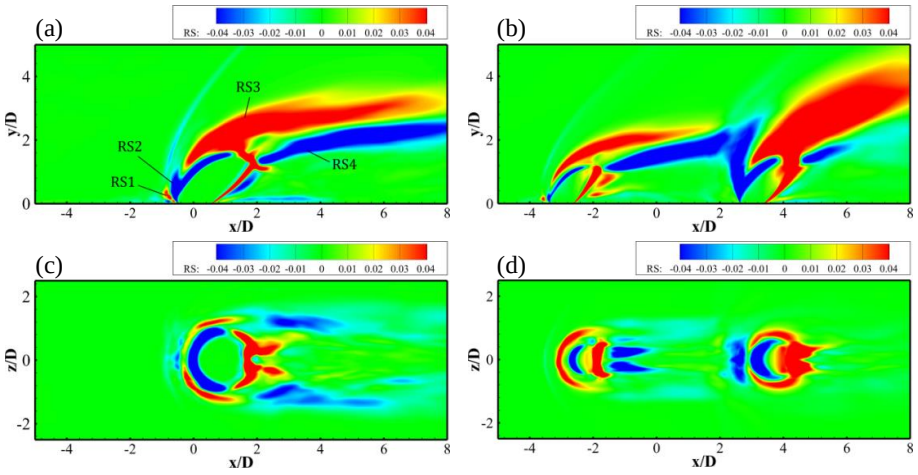

Fig. 15. Distributions of the Reynolds shear-stress: (a) z/D = 0 of single injection, (b) z/D = 0 of double injection, (c) y/D = 1 of single injection, (d) y/D = 1 of double injection.

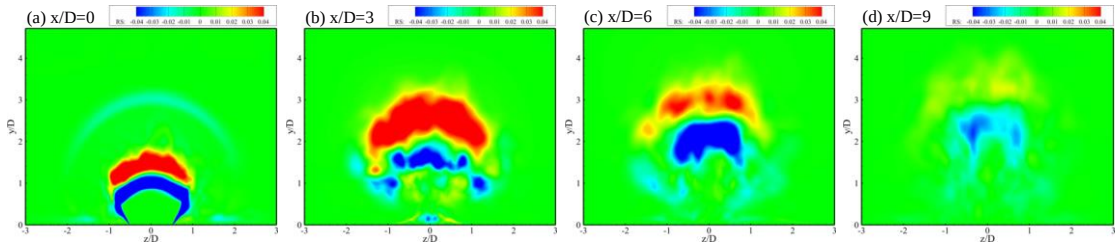

Fig. 16. Single injection: Reynolds shear stress distributions at different cross-sections.

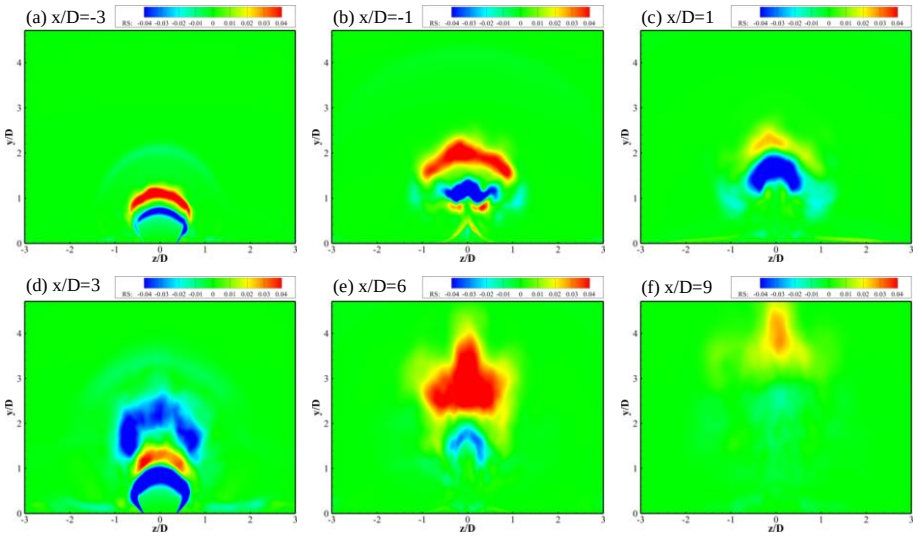

Fig. 17. Double injection: Reynolds shear stress distributions at different cross-sections.

3.5 Mixing Characteristics

Figure 18(a) depicts the maximum average hydrogen mass fraction versues x/D for the single/double jet cases. The maximum hydrogen mass fraction in the double injection has a rapidly decaying rate, which occurs downstream of the secondary injection due to interactions between the two

fuel injections and the multi-scale CVP downstream of secondary injection. On the other hand, the jet penetration depth is also one of the most important parameters to characterize the mixing process in JISC combustor [36, 38 & 39]. The jet penetration is defined as 1% of the average hydrogen mass fraction on the upwind side of the hydrogen jet flow in the symmetry plane (z/D=0) as suggested by Brown & Roshko [40]. Fig. 18(b) shows the predicted jet penetrations. Due to the influence of the primary injection, the penetration after the secondary injection is significantly greater than that in the single injection.

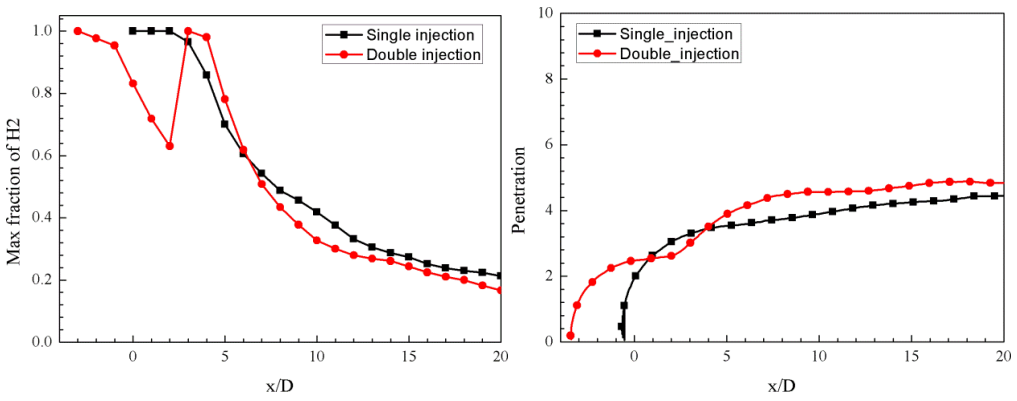

（a） （b）

Fig. 18. Attenuation of the maximum average hydrogen mass fraction (a); jet penetration (b).

The mixing efficiency η_{mix} and effective mixing area ratio ϕ are used to quantify the mixing characteristics of fuel jet and supersonic crossflow. The mixing efficiency is defined as the ratio of the effective mass flow rate of burnable hydrogen $\dot{m}_{mixed}$ to total hydrogen mass flow rate $\dot{m}_{total}$ at a given cross section [41 & 42]

$$\eta_{mix} = \frac{\dot{m}_{mixed}}{\dot{m}_{total}} = \frac{\int \alpha_{react} \rho u dA}{\int \alpha \rho u dA} \tag{3.1}$$

where,

$$\alpha_{react} = \begin{cases} \alpha, & \alpha \le \alpha_{stoic} \\ \alpha_{stoic} \dfrac{1-\alpha}{1-\alpha_{stoic}} & \alpha > \alpha_{stoic} \end{cases} \tag{3.2}$$

For the hydrogen jet in cross-flow, α is the average mass fraction of H_2 and α_{react} is the

average mass fraction of hydrogen that can be burned; ρuA represents the fluid mass flow rate at x-cross-section and A is the selected x-cross-section area; α_{stoic} is stoichiometric ratio of fuel hydrogen, which is 0.0283 in the present study. According to Hartfield et al. [43], the hydrogen mixture mole fraction of 4-75% indicates that it has been mixed, and the corresponding mass fraction is 0.0071-0.1135. The effective mixing area ratio is defined as [43]

$$\phi = \frac{\int \gamma dydz}{\int dydz}, \qquad \gamma = \begin{cases} 1, & if\ 0.0071 < \alpha < 0.1135 \\ 0, & else \end{cases} \tag{3.3}$$

Fig. 19 (a) and (b) show the jet mixing efficiency and the effective mixing area ratio along the streamwise direction. The mixing efficiency in the double injection is demonstrated to be much better than that in the single injection. With the double injection system, the mixing efficiency increases gradually after the primary injection, then decrease slightly after the secondary injection's presence. However, the mixing efficiency increases more rapidly after x/D = 4 for the double injection compared to the single injection. From the effective mixing area ratio analysis, seen in Fig. 19 (b), the near-field mixing area of the single injection is higher than that of the double injection, which is down to the higher jet mass flow rate of the single injection than the primary jet in the double injection in the near-field. However, after the secondary injection, the interaction between the primary injection and the secondary injection enhances the effective mixing area ratio after x/D>5 for the double injection.

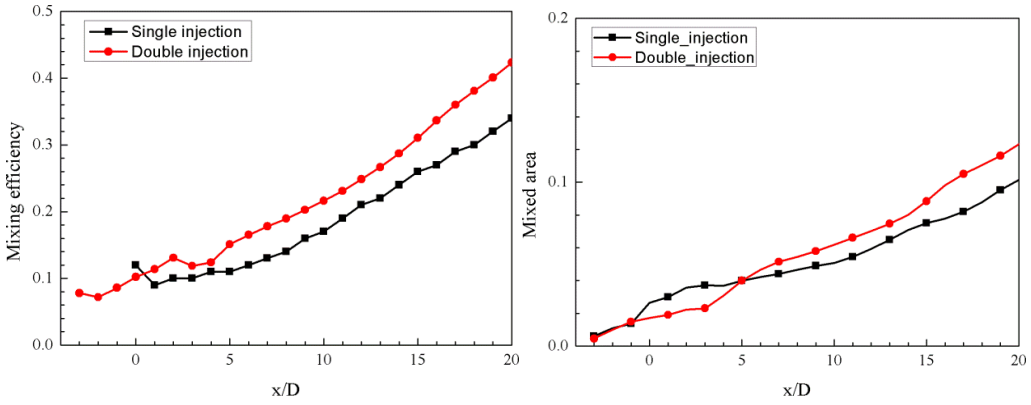

（a）Mixing Efficiency　　（b）Effective Mixing Area Ratio

Fig. 19. Mixing characteristics of the single and double injections.

Conclusions

Large-eddy simulations are performed to investigate the complex flow sturctures and mixing characteristics of the transverse sonic single/double hydrogen injection into supersonic crossflow. The main conclusions are as follows:

(1) In the double injection, the primary fuel jet fluid destroys the base of the bow shock on the windward side of the secondary injection and the jet shear layer vortex of the primary injection interacts and merges with those in the secondary jet flow, thereby changes the turbulence characteristics afterward. Besides, the hovering vortex between the secondary injection and its upstream recirculation zone disappears.

(2) Two-dimensional and three-dimensional streamlines demonstrate that the TCVP of the primary jet, the secondary TCVP and the horseshoe vortex of the secondary jet merge to form a new horseshoe vortex. Three pairs of CVP structures are generated downstream of the secondary jet: the first CVP-B is formed by the interaction of supersonic crossflow and secondary jet fluid; the second CVP-C is produced by the interactions of the supersonic crossflow, primary jet fluid and the secondary jet fluid; the third CVP-D is weak and formed by the interaction of the supersonic crossflow and primary jet fluid.

(3) The presence of primary jet flow alters the Reynolds shear stress distributions after the secondary injection. Transformation of the positive Reynolds shear stress region dominated by the jet shear layer and the negative Reynolds shear stress region dominated by the CVP can be observed in the double jet flow.

(4) The penetration and mixing efficiency of double injection system are significantly higher than that in the single injection system. The interaction between the primary injection and the secondary

injection yields an effective mixing area ratio after x/D>5 for the double injection.

Acknowledgment

This work is supported by the National Natural Science Foundation of China (Grant No. 91441117 and Grant No. 51576182). The numerical simulations in this paper have been performed on the supercomputers in the Supercomputing Center, University of Science and Technology of China.

References

[1] Mahesh K. The interaction of jets with crossflow[J]. Annual review of fluid mechanics, 2013, 45: 379-407.

[2] Jacobsen L S, Schetz J A, Ng W F. Flowfield near a mulitiport injector array in a supersonic flow[J]. Journal of Propulsion and Power, 2000, 16(2): 216-226.

[3] Murty, M. C., Bhandarkar, A. V., & Chakraborty, D. (2016). Aerothermal exploration of reaction control jet in supersonic crossflow at high altitude. Aerospace Science and Technology, 50, 266-271.

[4] Huang W, Wang ZG, Wu JP, Li SB. Numerical prediction on the interaction between the incident shock wave and the transverse slot injection in supersonic flows. Aerospace Science and Technology. 2013 Jul 1;28(1):91-9.

[5] Huang W. Transverse jet in supersonic crossflows[J]. Aerospace Science and Technology, 2016, 50: 183-195.

[6] Huang W. Effect of jet-to-crossflow pressure ratio arrangement on turbulent mixing in a flowpath with square staged injectors[J]. Fuel, 2015, 144: 164-170.

[7] Huang W, Liu J, Jin L, Yan L. Molecular weight and injector configuration effects on the transverse injection flow field properties in supersonic flows. Aerospace Science and Technology. 2014

Jan 1;32(1):94-102.

[8] Fallah K, Gerdroodbary MB, Ghaderi A, Alinejad J. The influence of micro air jets on mixing augmentation of fuel in cavity flameholder at supersonic flow. Aerospace Science and Technology. 2018 May 1;76:187-93.

[9] Lee S H. Characteristics of dual transverse injection in scramjet combustor, Part 1: Mixing[J]. Journal of Propulsion and Power, 2006, 22(5): 1012-1019.

[10] Huh J, Lee S. Numerical study on lateral jet interaction in supersonic crossflows. Aerospace Science and Technology. 2018 Jul 17.

[11] Lee S H. Characteristics of dual transverse injection in scramjet combustor, Part 2: Combustion[J]. Journal of Propulsion and Power, 2006, 22(5): 1020-1026.

[12] Takahashi H, Ikegami S, Masuya G, et al.. Extended quantitative fluorescence imaging for multicomponent and staged injection into supersonic crossflows[J]. Journal of Propulsion and Power, 2010, 26(4): 798-807.

[13] Takahashi, Hidemi, Goro Masuya, and Mitsutomo Hirota. "Supersonic Turbulent Mixing Structure in Staged Injection Flowfields." 48th AIAA Aerospace Sciences Meeting Including the New Horizons Forum and Aerospace Exposition. 2010.

[14] Pudsey A S, Boyce R R. Numerical investigation of transverse jets through multiport injector arrays in a supersonic crossflow[J]. Journal of Propulsion and Power, 2010, 26(6): 1225-1236.

[15] Pudsey A S, Boyce R R, Wheatley V. Hypersonic viscous drag reduction via multiporthole injector arrays[J]. Journal of Propulsion and Power, 2013, 29(5): 1087-1096.

[16] Micka D J, Driscoll J F. Combustion characteristics of a dual-mode scramjet combustor with cavity flameholder[J]. Proceedings of the combustion institute, 2009, 32(2): 2397-2404.

[17] Gerdroodbary M B, Amini Y, Ganji D D, et al. The flow feature of transverse hydrogen jet in presence of micro air jets in supersonic flow[J]. Advances in Space Research, 2017, 59(5): 1330-1340.

[18] Gerdroodbary M B, Fallah K, Pourmirzaagha H. Characteristics of transverse hydrogen jet in presence of multi air jets within scramjet combustor[J]. Acta Astronautica, 2017, 132: 25-32.

[19] Heidari A, Wen J X. Numerical simulation of flame acceleration and deflagration to detonation transition in hydrogen-air mixture[J]. International Journal of Hydrogen Energy, 2014, 39(36): 21317-21327.

[20] Maragkos G, Rauwoens P, Fauconnier D, et al. Large eddy simulations of differential molecular diffusion in non-reacting turbulent jets of H2/CO2 mixing with air[J]. Physics of Fluids (1994-present), 2014, 26(2): 025102.

[21] Garnier E, Adams N, Sagaut P. Large eddy simulation for compressible flows[M]. Springer Science & Business Media, 2009.

[22] Toda H B, Truffin K, Nicoud F. Is the dynamic procedure appropriate for all SGS model[C]//V European Conference on Computational Fluid Dynamics, ECCOMAS, Lisbon, Portugal. 2010: 14-17.

[23] Nicoud F, Ducros F. Subgrid-scale stress modelling based on the square of the velocity gradient tensor[J]. Flow, turbulence and Combustion, 1999, 62(3): 183-200.

[24] Zhao, M., Ye, T., Cao, C., Zhou, T., & Zhu, M. Study of sonic injection from circular injector into a supersonic cross-flow using large eddy simulation[J]. International journal of hydrogen energy, 2016, 41(39): 17657-17669.

[25] Zhao, M., Zhou, T., Ye, T., Zhu, M., & Zhang, H. Large eddy simulation of reacting flow in a hydrogen jet into supersonic cross-flow combustor with an inlet compression ramp[J]. International

Journal of Hydrogen Energy, 2017, 42(26): 16782-16792.

[26] Hoffman K A, Chiang S T. Computational Fluid Dynamics–Volume I. 4rd ed. Wichita Kansas: Engineering Education System. 2000; p.225-8.

[27] Ritos, Konstantinos, Ioannis W. Kokkinakis, and Dimitris Drikakis. "Physical insight into the accuracy of finely-resolved iLES in turbulent boundary layers." Computers & Fluids 169 (2018): 309-316.

[28] Drikakis, Dimitris, Marco Hahn, Andrew Mosedale, and Ben Thornber. "Large eddy simulation using high-resolution and high-order methods." Philosophical Transactions of the Royal Society A: Mathematical, Physical and Engineering Sciences 367, no. 1899 (2009): 2985-2997.

[29] Wang GL, Chen LW, Lu XY. Effects of the injector geometry on a sonic jet into a supersonic crossflow. Sci China Phys Mech Astronomy 2013;56(2):366e77.

[30] Bodony D J, Lele S K. On using large-eddy simulation for the prediction of noise from cold and heated turbulent jets[J]. Physics of Fluids, 2005, 17(8): 085103.

[31] Touber E. Unsteadiness in shock-wave/boundary layer interactions[D]. , 2010.

[32] Pope S B. Turbulent flows[J]. 2001.

[33] Ben-Yakar A, Mungal M G, Hanson R K. Time evolution and mixing characteristics of hydrogen and ethylene transverse jets in supersonic crossflows[J]. Physics of Fluids, 2006, 18(2): 026101.

[34] Kawai S, Lele S K. Large-eddy simulation of jet mixing in supersonic crossflows[J]. AIAA journal, 2010, 48(9): 2063-2083.

[35] Pudsey, Adrian S., Vincent Wheatley, and Russell R. Boyce. "Behavior of multiple-jet interactions in a hypersonic boundary layer." Journal of Propulsion and Power 31.1 (2014): 144-155.

[36] Santiago J G, Dutton J C. Velocity measurements of a jet injected into a supersonic crossflow[J]. Journal of Propulsion and Power, 1997, 13(2): 264-273.

[37] Rana, Zeeshan A., Ben Thornber, and Dimitris Drikakis. "Transverse jet injection into a supersonic turbulent cross-flow." Physics of Fluids 23.4 (2011): 046103.

[38] Ben-Yakar A, Hanson R. Ultra-fast-framing schlieren system for studies of the time evolution of jets in supersonic crossflows. Exp Fluids 2002;32(6):652-66.

[39] Chai X, Iyer PS, Mahesh K. Numerical study of high speed jets in crossflow. J Fluid Mech 2015;785:152-88.

[40] Brown G L, Roshko A. On density effects and large structure in turbulent mixing layers[J]. Journal of Fluid Mechanics, 1974, 64(4): 775-816.

[41] Sislian JP, Schumacher J. Fuel/air mixing enhancement by cantilevered ramp injectors in hypersonic flows[C]// International Society for air breathing engines- ISOABE, ISABE e International Symposium on air breathing engines, 14 th, Florence, Italy. 1999.

[42] Li L, Huang W, Yan L. Mixing augmentation induced by a vortex generator located upstream of the transverse gaseous jet in supersonic flows[J]. Aerospace Science and Technology, 2017, 68: 77-89.

[43] Hartfield R J, Hollo S D, McDaniel J C. Experimental investigation of a supersonic swept ramp injector using laser-induced iodine fluorescence[J]. Journal of propulsion and power, 1994, 10(1): 129-135.